scientific reports

Check for updates

OPEN

Efficient adsorption of bisphenol A using magnetically recyclable nanocomposites with Box Behnken optimization

Chou-Yi Hsu[1], Ebraheem Abdu Musad Saleh[2], Nusiba M. M. Alshik[2], Mohammed Asiri[3], Sandeep Singh[4,10], Abhayveer Singh[5], V. Kavitha[6], Mehul Manu[7], Nezamaddin Mengelizadeh[8] & Davoud Balarak[9]✉

The study focused on evaluating the adsorption potential of Fe_3O_4/ZIF-8 (MFZ) for Bisphenol A (BPA) removal from aqueous environments. Different physicochemical factors, encompassing pH, Fe_3O_4/ZIF-8 dose, mixing time and temperature exerted an impact on the adsorption process. The adsorbent was characterized by Scanning Electron Microscopy (SEM), Vibrating Sample Magnetometry (VSM), Thermogravimetric Analysis (TGA), Brunauer–Emmett–Teller (BET) analysis, X-ray Photoelectron Spectroscopy (XPS), Fourier-Transform Infrared Spectroscopy (FT-IR), and X-ray Diffraction (XRD). Using Response Surface Methodology (RSM), experimental data underwent optimization through a Box–Behnken Design (BBD) with 29 trials. The quadratic model, with a maximum R^2 (0.995), emerged as the best fit, delineating a suitable relationship between the variables and the response. The optimum conditions for BPA removal by MFZ, determined by the model, were detected to be a pH of 6.2, an adsorbent dose of 0.75 g/L, a mixing time of 72 min, and a temperature of 315 K, yielding an anticipated percentage removal of 99.1. Experimental validation under these conditions showed a percentage removal of 98.9%, deviating only 0.2% from the predicted value. In the presence of NaCl, Na_2SO_4, Na_2CO_3, $NaNO_3$, varying degrees of inhibition are observed in the adsorption effectiveness of MFZ on BPA. Across the five regeneration cycles, the percentage removal of MFZ for BPA experienced a slight decrease. The results suggest that the removal of BPA ions is notably influenced by the adsorption conditions.

Keywords RSM, Bisphenol a, Optimization, Box–Behnken design, Fe_3O_4/ZIF-8, Magnetically recyclable

In recent decades, rapid urbanization and human activities have propelled concerns regarding the safety and quality of drinking water[1]. The alarming rise of micro-contaminants, particularly endocrine-disrupting compounds (EDCs), has heightened the urgency for safe and clean drinking water[2,3]. BPA stands out as a prominent EDC, serving as a crucial raw material in the production of food cans, polycarbonate plastics, epoxy resins, thermal paper, polyester fibers, and various industrial materials[4,5]. BPA pervasive presence in everyday items like water pipes, toys, paper, and electronic equipment has made it a ubiquitous synthetic chemical[6]. Its global production exceeds three million tons annually, highlighting the widespread use of this compound. Since then, BPA has been classified as a significant water contaminant in various regions across the globe[7,8]. Various sources contribute to exposure to BPA, such as dental fissure sealants, adhesives, household dust, and printing

[1]Department of Pharmacy, Chia Nan University of Pharmacy and Science, Tainan 71710, Taiwan. [2]Department of Chemistry, College of Science and Humanities in Al-Kharj, Prince Sattam Bin Abdulaziz University, 11942 Al-Kharj, Saudi Arabia. [3]Department of Clinical Laboratory Sciences, College of Applied Medical Sciences, King Khalid University, Abha, Saudi Arabia. [4]School of Engineering and Technology, CGC University, Mohali, 140307, India. [5]Centre for Research Impact & Outcome, Chitkara University Institute of Engineering and Technology, Chitkara University, Rajpura, Punjab 140401, India. [6]Department of Chemistry, Sathyabama Institute of Science and Technology, Chennai, Tamil Nadu, India. [7]Department of Allied Science (Physics), Graphic Era Hill University, Bhimtal, India. [8]Department of Environmental Health Engineering, Evas Faculty of Health, Larestan University of Medical Sciences, Larestan, Iran. [9]Department of Environmental Health, Health Promotion Research Center, Zahedan University of Medical Sciences, Zahedan, Iran. [10] Faculty of Engineering, Sohar University, Sohar, Oman. ✉email: dbalarak2@gmail.com

inks, tableware, polycarbonate bottles (often utilized for newborn formula milk), epoxy resin coatings in food and beverage containers[9,10]. The issue is further exacerbated when BPA-containing plastic containers hydrolyze and contaminate groundwater through landfill leachate, as plastic industries discharge substantial amounts of BPA into the environment[11,12]. Unfortunately, BPA's ecological impacts extend beyond environmental contamination. Even at minuscule concentrations, BPA can disrupt the hormone systems of animals and humans, posing a significant health risk[13,14]. The estrogenic activity of this substance has implications for health, connecting it to issues like effects on the immune system, heart disease, reproductive challenges, disturbances in normal hormone functions, neurological complications, diabetes, obesity, tumors, and cancer[15,16]. Moreover, BPA exhibits biomagnification and bioaccumulation through the food chain, posing an even greater threat to human health[17]. The long-term dysfunction and damage caused by BPA underscore the urgent need for its removal from water sources[18].

Several methods, including biological treatment, redox reactions, membrane filtration, coagulation, and adsorption, have been investigated for BPA removal[19]. Nevertheless, each of these techniques presents notable drawbacks: biological treatments are generally slow and ineffective at trace BPA concentrations; redox reactions require strong oxidants or costly catalysts and may lead to the formation of harmful by-products; membrane filtration ensures effective separation but suffers from fouling, high operating pressure, and significant cost; while coagulation results in the generation of large amounts of chemical sludge, posing challenges for handling and disposal[20]. Adsorption stands out as a promising wastewater purification method due to its simplicity, energy efficiency, and effectiveness[21]. Various adsorbents, e.g., chitosan, activated carbon, multi walled carbon nanotubes, and composite materials, have exhibited efficient elimination of BPA[22,23]. Adsorption applications hold great promise, but the capacity and sustainability of materials used in these applications are hampered by a number of factors such as limitations in preparation processes, structural adaptability, specific surface area, and surface chemical activity[24,25]. Conventional carbon adsorbents often require energy-intensive activation, while powdered nano-adsorbents face agglomeration issues that impede mass transfer and reusability[26]. An ideal adsorbent should possess an extensive specific surface area, rich pore structure, high-affinity adsorption sites, and convenient separation features to facilitate efficient phenol removal[27].

Metal-organic frameworks (MOFs) are unique porous coordination polymers comprising an organized three-dimensional network formed by organic ligands and metal ions or clusters[28]. Their ultra-high specific surface area, regular pores, high mechanical stability, and design flexibility make MOFs superior candidates for phenol removal. Among these, ZIF-8, a sodalite-type zinc imidazole, stands out[29]. Its tetrahedrally coordinated imidazolate linkers create large cavities, providing ample space for phenol adsorption. ZIF-8 demonstrates exceptional thermal, water, and alkali stability in aqueous solutions, enhancing its practical application[30]. Despite its promising features, ZIF-8's microcrystalline powder characteristic poses challenges in separation and recovery, potentially causing secondary environmental pollution[31]. Some researchers have attempted to address this by combining MOFs with membrane materials. Nevertheless, the fragile bond between the membrane substrate MOF remains a significant challenge, and the introduction of a membrane supporter with limited adsorption capacity can reduce overall efficiency[31]. Addressing the drawback of difficult separation, magnetizing adsorbents introduces a novel application in engineering separation. Magnetic separation proves effective in recovering powdered adsorbents from solutions, with magnetic nanoparticles demonstrating proficiency in removing various environmental pollutants[32]. Combining magnetic particles with MOFs facilitates easy and efficient separation through an external magnetic field. Researchers have explored core–shell structured magnetic MOFs, where a magnetic core is enclosed by a thin MOF layer[27]. While this structure may typically increase adsorbent density and decrease adsorption volume, leading to reduced capacity, the incorporation of small-sized (> 10 nm) Fe_3O_4 nanoparticles (Fe_3O_4 NPs) into the ZIF-8 adsorbent mitigates these issues[30]. This approach leverages the adsorption benefits of ZIF-8 and the magnetic responsiveness of Fe_3O_4 NPs while minimizing mutual interference[29]. The resulting composite adsorbent maintains high adsorption capacity and recoverability. Thus, the integration of multiple strategies has resulted in the development of a highly efficient and eco-friendly adsorbent. This innovative approach holds great promise for the future of adsorbent technology[33].

The novelty of the present study lies in the design and synthesis of a magnetically recyclable MFZ nanocomposite specifically tailored for the removal of BPA, a hazardous endocrine-disrupting compound. Although magnetic MOF-based composites have been reported previously, most of them have focused on heavy metals or dyes, and only limited attention has been given to BPA despite its high environmental and health relevance. In this work, a modified synthesis strategy was adopted to integrate Fe_3O_4 nanoparticles into the ZIF-8 framework, ensuring improved stability, smaller crystallite size, and rapid magnetic separability. In addition, unlike conventional one-factor-at-a-time approaches, the adsorption process in this study was systematically investigated using RSM with a BBD, which allows for comprehensive multi-parameter optimization and a deeper understanding of interaction effects. Moreover, the potential influence of coexisting ions, commonly present in real water matrices, was also considered to better evaluate the applicability of the proposed adsorbent. These aspects collectively distinguish this study from previous works and establish its novelty in both material development and methodological approach.

MFZ nanocomposites offer a distinct advantage as adsorbents, since they combine the high surface area and abundant active sites of ZIF-8 with the facile magnetic separability of Fe_3O_4 nanoparticles, making them both highly efficient for pollutant removal and easily recoverable for repeated use. Thus, this study focuses on assessing the BPA adsorption by MFZ. The research investigates the impact of different parameters (pH, temperature, adsorbent dosage, and mixing time) on the BPA adsorption. Additionally, RSM using the BBD is employed to understand the influence of independent components and their interactions, leading to the development of an optimized mathematical model for identifying the most favorable conditions for adsorption. Finally, the study examines the potential for reusing MFZ and evaluates the practical application feasibility of the material by analyzing production costs.

Materials and methods

Reagents

The substances, including nitric acid (HNO_3, 65–68%), zinc nitrate hexahydrate ($Zn(NO_3)_2.6H_2O$, 99%), 2-methylimidazole ($C_4H_6N_2$, 98%), ferric tetroxide (Fe_3O_4, 97%, particle size 50–300 nm), Bisphenol A (BPA), sodium hydroxide (NaOH, 96%), hydrochloric acid (HCl, 37%), anhydrous methanol (CH_3OH, 99.5%), and poly (sodium 4-styrenesulfonate) $(C_8H_9NaO_3S)_n$, were supplied by Merck Co., Germany. All remaining materials (NaCl, Na_2SO_4, Na_2CO_3, and $NaNO_3$) were obtained from Sigma Aldrich, USA. No further purification was necessary, and the reagents were used in their received form.

Adsorbent preparation

ZIF-8 synthesis

In solution A, nitrate hexahydrate (1.5 g) was dissolved in 40 mL of anhydrous methanol, while solution B was prepared by dissolving 2-methylimidazole (3.3 g) in anhydrous methanol (40 mL). After mixing the above solutions for half an hour, the gradual addition of solution B to Solution A took place, followed by vigorous stirring for 3 h. Subsequently, the mixture was allowed to stand at room temperature for a day. The turbid solution then underwent centrifugation at 6,000 rpm; the resulting solid was washed with anhydrous methanol. The subsequent step involved drying the solid for 12 h at 60 °C in a vacuum oven, leading to the production of a ZIF-8 powder sample.

MFZ synthesis

In this study, the synthesis of MFZ was based on an in-situ precipitation/coating approach, where ZIF-8 was directly grown on the surface of Fe_2O_4 nanoparticles[31]. Initially, a solution was prepared by dissolving poly (sodium 4-styrenesulfonate) (PSS; 1.0 g) in double-distilled water (100 mL), followed by sonication using an ultrasonic bath (model SK2210HP, China) for 30 min to achieve a uniform and translucent solution. Subsequently, Fe_3O_4 nanoparticles (0.5 g) were introduced into the PSS solution, undergoing 30-minute of sonication process before magnetic separation and triple washes with double-distilled water. The formed Fe_3O_4 particles were combined with a methanol solution containing 2-methylimidazole (1.1 g) and $Zn(NO_3)_2{\cdot}H_2O$. After three hours of stirring, the obtained MFZ particles were isolated by magnetic separation, washed thoroughly with methanol, and dried overnight at 80 °C (see the schematic in Fig. 1).

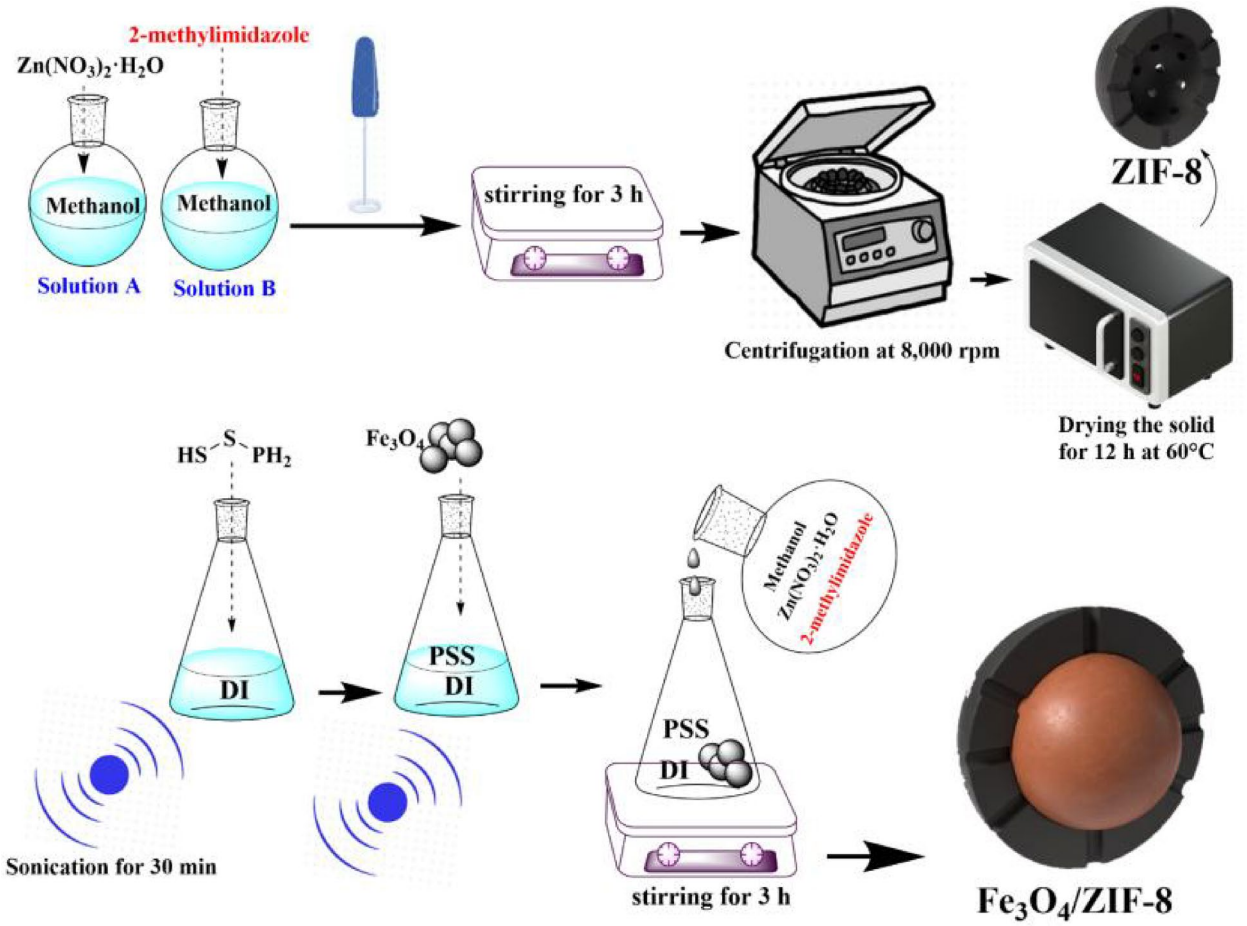

Fig. 1. Schematic of synthesis of MFZ by precipitation method.

Characterization of adsorbents

The FTIR spectra were recorded using a Bruker Tensor II FTIR spectrometer in the range of 400–4000 1/cm. The XRD patterns were obtained on a Rigaku Ultima IV X-ray diffractometer using Cu Kα radiation (λ = 1.5406 Å) over a 2θ range of 10–80°. The thermal stability of the adsorbents was measured using thermogravimetric analysis. The analysis was performed using a Mettler Toledo analyzer. The specific surface area and pore volume of the adsorbents were determined using an automated gas sorption system that employed a BET NOVA 1200 surface area and pore size analyzer from Quantachrome Instrument. Investigating magnetic properties of the samples was done using vibrating sample magnetometry, which was conducted using a PPMS-9 T device from Quan-tum Design, USA. The magnetic properties were analyzed over a range of 20 to 20 kOe. The SEM analysis was carried out by using a TESCAN MIRA3 device from Czech Republic. The XPS analysis was carried out using an ESCALAB 250Xi spectrometer (Thermo Scientific, USA) equipped with a monochromatic Al Kα radiation source.

Batch adsorption experiments

Experiments were carried out in batches to found the most favorable conditions for eliminating BPA. The experiments involved mixing a 100 mL solution of BPA (100 mg/L) with a known quantity of MFZ in a 250 mL flask. The resulting mixture was mechanically shaken using a rotary shaker (Dragon LAB, skp-0330-pro-Germany) at 180 rpm. Various experimental parameters, such as pH, adsorbent dosage, and temperature, were investigated to determine their impact on BPA removal efficiency. The initial pH was adjusted using either 0.1 M HCl or 0.1 M NaOH solutions, and a pH meter was used for this purpose. After 60 min of shaking, samples were removed from the solution and the MFZ was separated from the supernatant using a magnet. The concentration of the target analyte was determined using a Knauer HPLC 862 system equipped with a SPD-20 A UV–Vis detector and a C18 column (250 × 4.6 mm, 5 µm particle size). The mobile phase consisted of a 50:50 (v/v) mixture of ammonium acetate and methanol.

The mobile phase flow rate was set at 0.9 mL/min, and the wavelength used was 225 nm. Additionally, the impact of various ions, such as NaCl, Na_2SO_4, Na_2CO_3, and $NaNO_3$, at a concentration of 10 mg/L on BPA adsorption by MFZ was investigated. The COD of the wastewater was determined using the closed reflux spectrophotometric method with standard COD digestion vials. The samples were digested at 150 °C for 2 h in a COD reactor, and the absorbance was measured at 600 nm using a Hach DR 5000 UV-Vis Spectrophotometer.

The equation below was employed to determine the BPA removal efficiency, represented as R (%)[34]:

$$Adsorption\ percentage(\%) = \frac{\mathrm{Co} - \mathrm{Ce}}{\mathrm{Co}} \times 100 \tag{1}$$

The equation used to determine the adsorption capacity (q_e, mg/g) at equilibrium is as follows[35]:

$$\mathrm{Q}e = \left(\frac{\mathrm{Co} - \mathrm{Ce}}{M} \times V\right) \tag{2}$$

In the context of the BPA adsorption process, C_0 denotes the initial concentration, while $C_e$represents the equilibrium concentration, both expressed in mg/L. The variables V (L) and m (g/L) refer to the volume of the BPA solution and the mass of the MFZ, respectively.

RSM optimization

In the realm of RSM, a predefined set of experiments is conducted to achieve a response with a limited number of trials. This statistical approach is particularly apt for multi-factor experiments, unraveling the connections among diverse parameters to establish optimal operational conditions. The determination of the number of experimental runs (N) in RSM involves the utilization of the following Eq. (38):

$$N = 2K \times\ (K - 1) +\ C_0 \tag{3}$$

where K = Number of variables and Co = Centre-point. The following quadratic equation explains the behavior of the system:

$$Y = \beta_0 + \sum_{i=1}^{K} \beta_i X_i + \sum_{i=1}^{K} \beta_{ii} X_i^2 + \sum_{i=1 \le i \le j}^{K} \beta_{ij} X_i X_{j+\varepsilon} \tag{4}$$

where Y = Predicted response, β_0 = Constant coefficient, βi = Linear coefficient, βii = Quadratic, βij = Interactive coefficients and ε = Error of the model.

Graphical representations, such as contour plots and surface plots, illustrate the response, highlighting interaction effects among the main factors and optimal system conditions. Employing Design Expert 10 software, an experimental design was formulated to assess the combined influence of four independent input variables through sets of experiments. The experimentation involved running five tests at central points, with process parameters set at three different levels as described in Table 1. The process parameters were considered independent variables, while the maximum adsorption capacity was identified as the output response variable. This method is an efficient way to explore the effects of various process parameters on adsorption with a limited number of experiments.

Variable	Sign	Levels			
		Unit	−1	0	1
pH	A	–	4	7	10
MFZ dosage	B	g/L	0.2	0.6	1
Contact time	C	min	30	60	90
Temperature	D	°C	10	25	40

Table 1. Experimental design levels of chosen variables.

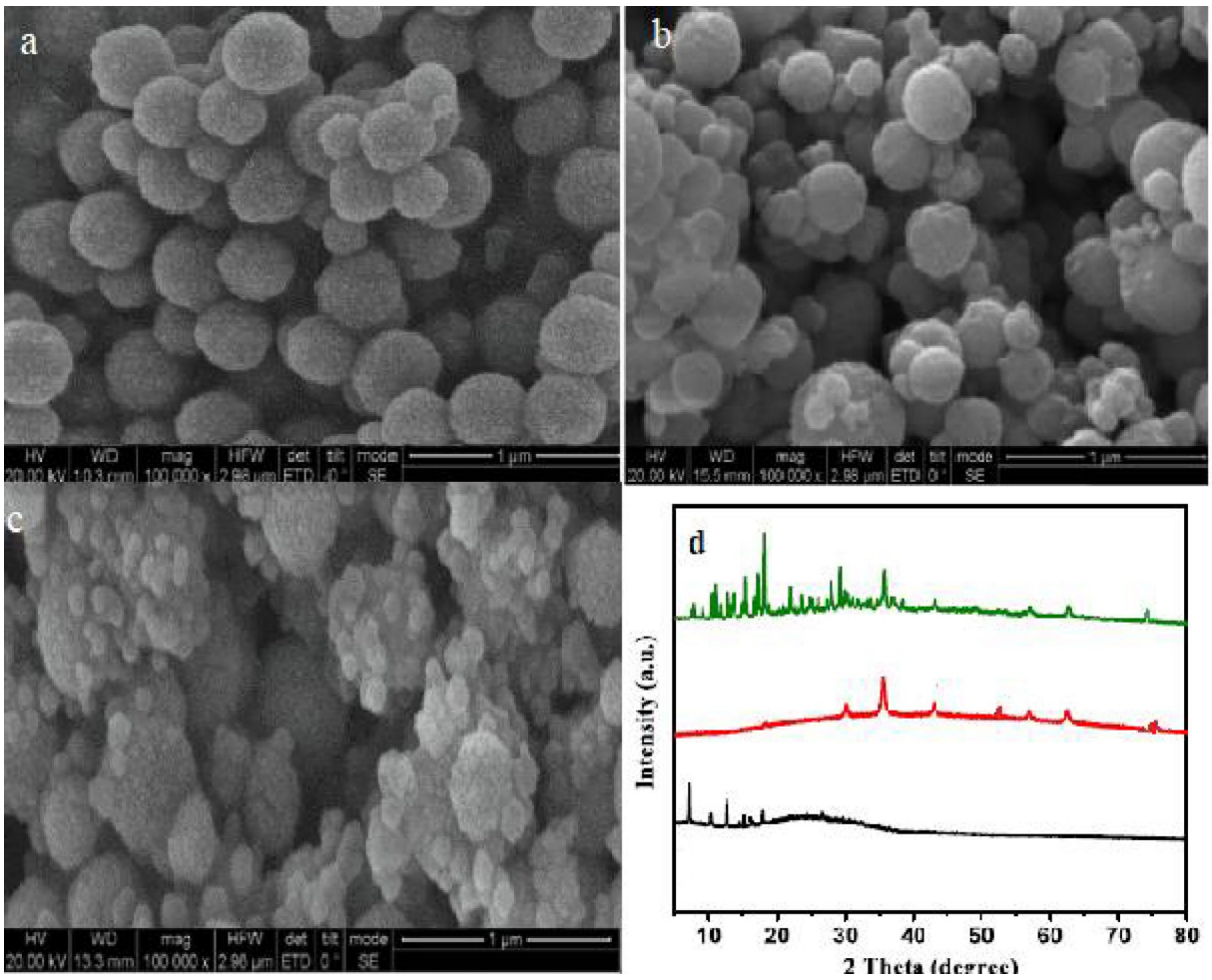

Fig. 2. SEM images of ZIF-8 (**a**), Fe_3O_4 (**b**), MFZ (**c**); XRD patterns (**d**).

Considering the removal efficiency of BPA as the dependent variable (response), Table 1 provides details on the four factors studied, including their chosen levels and associated ranges. To ensure experiment reproducibility, all experiments were conducted with three replications, with a criterion of relative standard deviation (RSD) less than 0.05. Central points were chosen for estimating and gauging experimental error, as well as gauging the lack of fit (LOF). LOF was employed, along with an examination of R^2 and R^2 Adj between laboratory and predicted values, to ascertain the statistical significance of quadratic fit models.

Results and discussion

Characterization of adsorbent

Figure 2a, b and c depict SEM images of ZIF-8, Fe_3O_4, and MFZ. In the SEM images, ZIF-8 shows a polyhedral morphology that corresponds to its sodalite-type crystal structure. After the incorporation of Fe_2O_4 nanoparticles, however, the MFZ composite exhibits a less regular shape, where many particles appear nearly spherical due to the coating of Fe_2O_4 on the ZIF-8 surface and partial aggregation during synthesis. This morphological change is significant for adsorption. The combination of polyhedral ZIF-8 crystals and spherical-like Fe_2O_4 domains provides a hierarchical surface, which increases surface roughness, creates additional active adsorption sites, and

facilitates π–π interactions and hydrogen bonding with BPA molecules[33]. Moreover, the spherical Fe_2O_4 particles improve dispersion and magnetic separability, while ZIF-8 contributes microporous channels with high surface area. Together, these features enhance both the adsorption capacity and the recyclability of the composite.

Figure 2d displays the XRD patterns of Fe_3O_4, ZIF-8, and MFZ. The XRD patterns of the samples were compared with the reference data from the JCPDS database to identify the crystalline phases. The characteristic peaks of ZIF-8 appeared at 2θ values of 7.5°, 10.5°, 12.5°, 14.7°, 16.2°, and 18.0°, corresponding to the (011), (002), (112), (022), (013), and (222) planes, which are in good agreement with the standard card JCPDS No. 00-062-1030. In addition, the diffraction peaks of Fe_2O_4 were observed at 2θ values of 30.3°, 35.5°, 43.3°, 53.4°, 56.9°, 62.7°, and 74.0°, indexed to the (220), (311), (400), (422), (511), (440), and (533) planes of JCPDS No. 00-019-0629. The coexistence of both sets of diffraction peaks in the MFZ pattern confirms the successful formation of the composite structure, demonstrating that the crystalline framework of ZIF-8 was preserved during synthesis while Fe_2O_4 nanoparticles were effectively incorporated.

The Debye–Scherrer Eq. (5) uses for to estimate the crystallite sizes of the MFZ[32].

$$D = \frac{0.89\ \lambda}{\beta \cos\ \theta} \tag{5}$$

The Debye–Scherrer equation involves several variables. The shape factor is represented by 0.89, and D represents the average particle size. λ refers to the wavelength of the Cu Kα irradiation. β represents the full width at half maximum intensity of the diffraction peak obtained. θ is the diffraction angle of the (311) peak of the MFZ MNPs. The calculated size of the MFZ's crystallite is approximately 6.6 nm.

As depicted in Fig. 3a, representing N_2 adsorption/desorption isotherms and pore size distributions for desired samples, ZIF-8 showcases a type-I isotherm, whereas MFZ demonstrates a type-IV isotherm, emphasizing the notable presence of micropores in the ZIF-8 structure[32]. Additionally, MFZ displays an H_4-type hysteresis loop within the 0.45 < P/P0 < 1.0 range, signifying a hierarchical porous structure encompassing both micropores and mesopores. After the introduction of Fe_3O_4, specific surface area of MFZ is measured at 421.3 m^2/g, a notable reduction compared to the original ZIF-8 (711.2 m^2/g). The reason for the reduction is ascribed to the inclusion of Fe_3O_4 particles that are heavier and non-porous[36]. However, despite this reduction, the introduction of Fe_3O_4 does not compromise the adsorption properties of ZIF-8. MFZ displays a diminished pore capacity of 0.352 cm^3/g in contrast to ZIF-8 (0.434 cm^3/g), primarily due to the presence of Fe_3O_4 particles inside ZIF-8[32]. The pore size distributions, calculated with the BJH method, are outlined in Fig. 3a. These distributions reveal a confined range of pore sizes, specifically between 3 nm and 10 nm, indicating a highly uniform pore structure for both ZIF-8 and MFZ nanoparticles.

The magnetic properties of Fe_3O_4 and MFZ were examined using a vibrating sample magnetometer (VSM), and the corresponding VSM curves are illustrated in Fig. 3b. Remarkably, both samples display an absence of coercivity or hysteresis effect at room temperature, indicating their superparamagnetic behavior. The magnetization strengths of Fe_3O_4 and MFZ are measured at 64.2 and 18.4 emu/g, respectively. Although MFZ exhibits a considerably lower magnetization strength compared to Fe_3O_4, when subjected to an external magnet, separation of MFZ is swiftly done from water within 10 s. The reduction in magnetic strength for the composite can be explained by its lower non-magnetic characteristics of ZIF-8 and Fe_3O_4 content, leading to a lessened magnetization[33]. Overall, the incorporation of Fe_3O_4 particles imparts magnetic properties to the composite, facilitating efficient retrieval from water through magnetic separation and regeneration, thereby reducing overall process costs.

In the FTIR spectra (Fig. 3c), the peaks that are unique and specific to the stretching vibration absorption of C-H can be seen at 2927 and 3141 1/cm. These peaks correspond respectively to the C-H bond of the saturated hydrocarbon (CH_3) and the C-H bond of the unsaturated hydrocarbon of 2-methylimidazole[36]. Notably, the absence of broad peaks in the wavenumber range of 3300 to 3500 1/cm is indicative of Zn binding to N-H on the 2-methylimidazole ligand. The sharp peak at 446 1/cm is attributed to the stretching vibration of Zn-N, signifying successful linkage of Zn to N. Additionally, a new characteristic peak at 554 1/cm in the MFZ spectrum is attributed to the stretching vibration of Fe–O, confirming the successful combination of Fe_3O_4 and ZIF-8. At 3465 1/cm, the samples exhibit wide spectral regions that correspond to the stretching and bending oscillations of –OH groups[31]. In the 700–1600 1/cm range, the characteristic peak represents the 2-methylimidazole ligand, with the stretching vibration peak of the C=N bond in the imidazole ring observed at 1540 1/cm, indicating that the presence of Fe_3O_4 does not lead to the disappearance of the 2-methylimidazole organic ligand[32]. This suggests that functional groups on the composite, including Fe–O, Zn–N, and C=N, offer abundant active sites for BPA removal.

As evidenced by the TGA curves obtained under N_2 atmosphere (Fig. 3d), outstanding thermal stability could be detected for ZIF-8 and MFZ. At 150–450 °C, both ZIF-8 and MFZ experience weight loss, with ZIF-8 losing 13.1% and MFZ losing 9.9%. This weight loss is linked to residual water, organic solvent, and unreacted 2-methyl imidazole[35]. Notably, MFZ, with its lower porosity and reduced residual water and chemical solvents, exhibits less weight loss than ZIF-8. As the temperature rises, the weights of both adsorbents decrease rapidly due to the breaking of Zn-N bonds and the failure of the organic structure. The incorporation of Fe_3O_4 in the MFZ composite has been found to improve its thermal stability compared to that of ZIF-8. This enhancement is assigned to the incorporation of magnetic nanoparticles, which contribute to the composite's increased stability[34]. Nevertheless, the thermal stabilities of both adsorbents remain robust, in accordance with prior studies on ZIF-8.

The XPS survey spectrum (Fig. 4a) confirms the coexistence of C, N, O, Fe, and Zn elements, demonstrating the successful formation of the Fe_2O_4/ZIF-8 composite. The high-resolution C 1s spectrum (Fig. 4b) exhibits dominant peaks at 284.8 eV and 285.6 eV, corresponding to C–C/C–H and C–N bonds, respectively, which

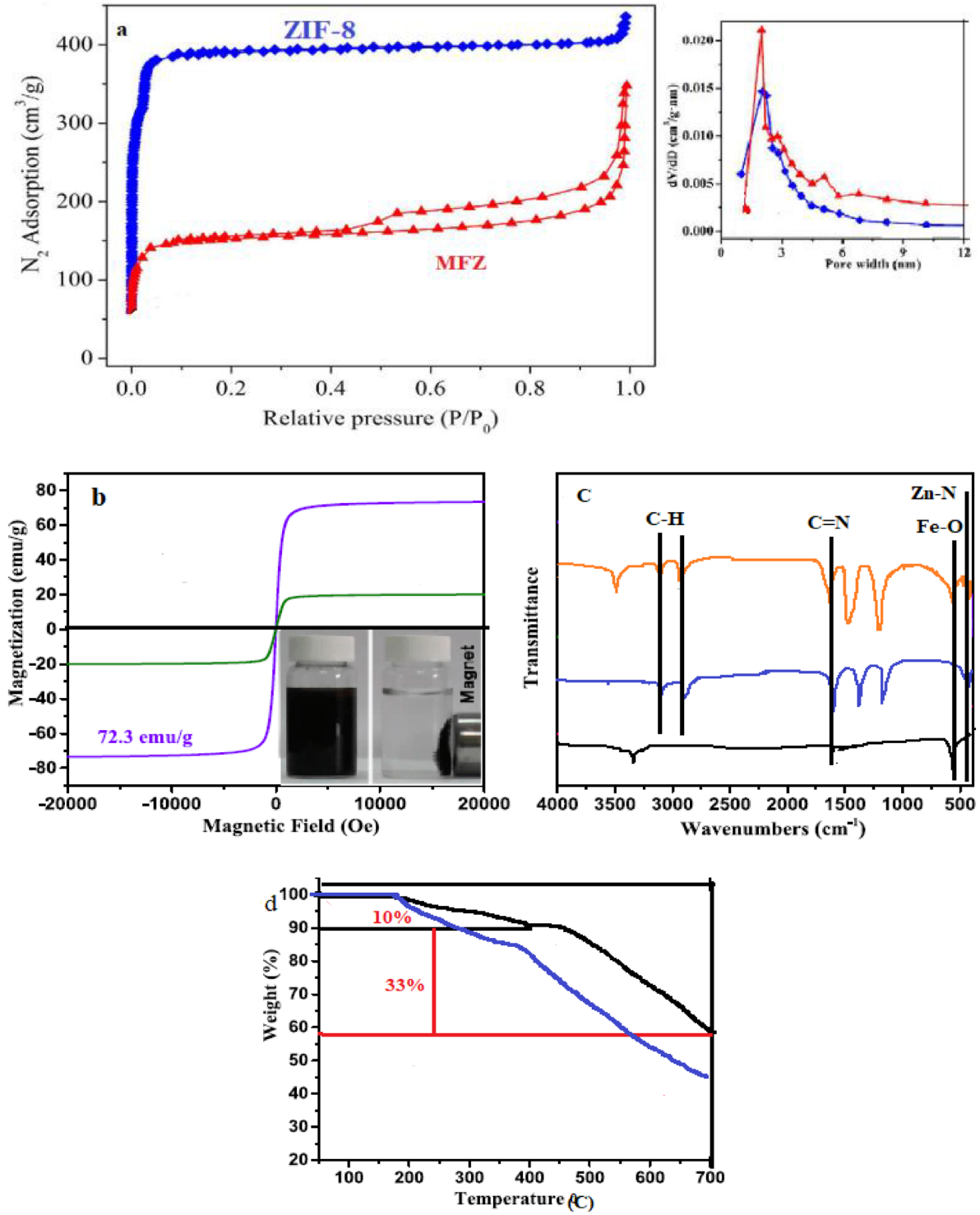

Fig. 3. Nitrogen adsorption desorption isotherms and pore size distributions (**a**); VSM magnetization curves of ZIF-8 and MFZ (**b**); FTIR spectra (**c**) and TGA profiles of ZIF-8 and MFZ (**d**).

originate from the organic imidazolate linker of ZIF-8. The N 1s spectrum (Fig. 4c) shows two components at ~398.6 eV and ~399.7 eV, assigned to pyridinic-N and Zn–N species, further confirming the coordination of Zn^{2+} with nitrogen atoms in the framework. In the O 1s region (Fig. 4d), the deconvolution reveals contributions at ~530.2 eV and ~531.6 eV, associated with Fe–O and Zn–O bonds, indicating the coexistence and interfacial interaction of Fe_2O_4 and ZIF-8. The Zn 2p spectrum (Fig. 4e) displays two characteristic peaks at 1021.6 eV (Zn $2p_2/_2$) and 1044.7 eV (Zn $2p_1/_2$), consistent with Zn^{2+} species in ZIF-8. Meanwhile, the Fe 2p spectrum (survey, inset) shows the coexistence of Fe^{2+} and Fe^{3+}, characteristic of Fe_2O_4. Altogether, these results confirm

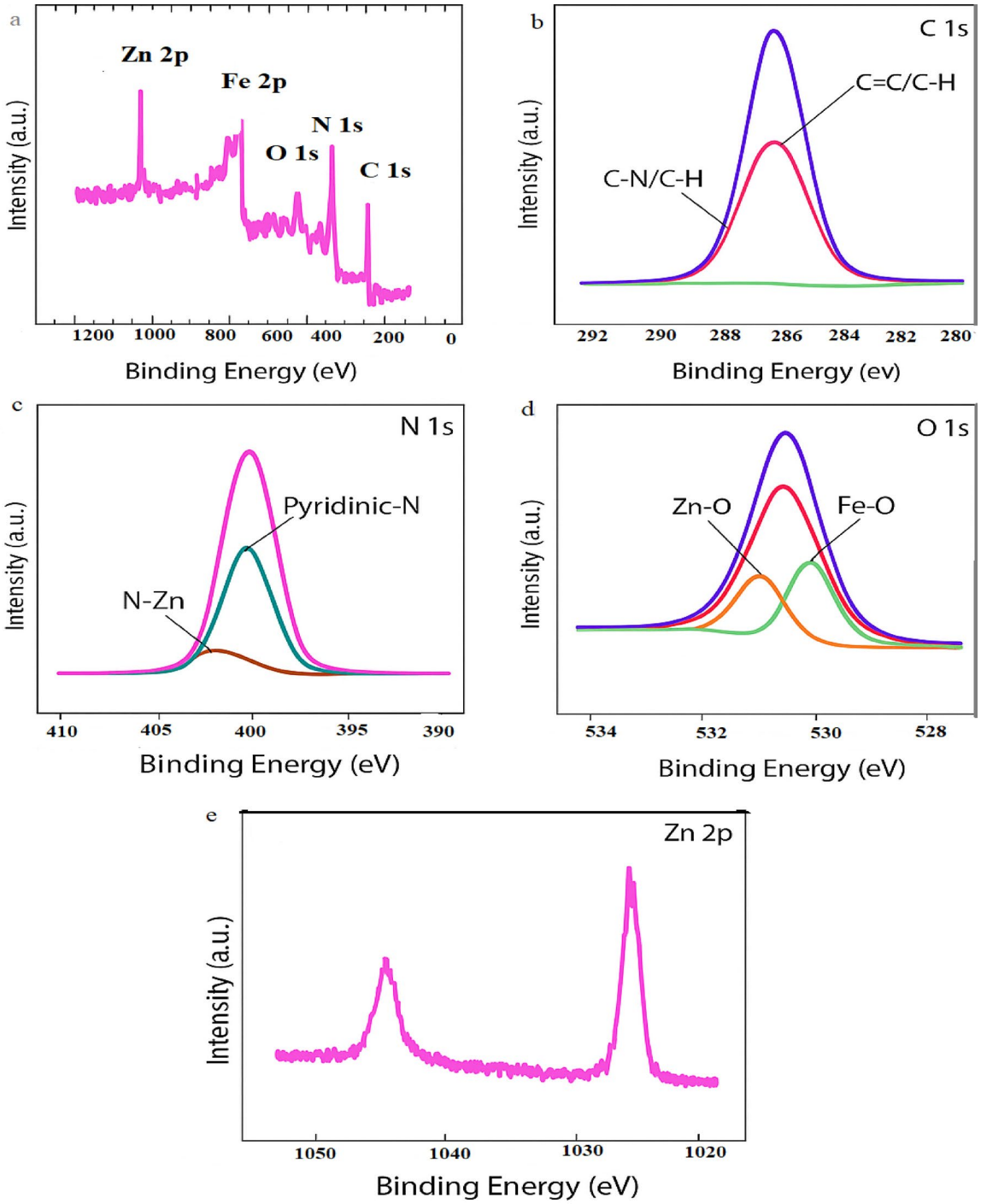

Fig. 4. XPS spectra of MFZ (**a**); (b) C 1s; (**b**) N 1s; (**c**) O 1s; (**d**) Zn 2p (**e**).

the successful integration of Fe_2O_4 with the ZIF-8 framework and suggest strong chemical interactions between the two components.

RSM optimization

The relationships between BPA removal percentage, MFZ mass, contact time, pH, and temperature were established using the BBD model, which employed four models. To explain the connections between the removal percentage of BPA and the adsorbent mass, contact time, pH, and temperature, the quadratic polynomial model was specifically utilized. Based on the obtained results, the equation representing the quadratic polynomial model for the adsorption capacity of BPA is expressed by Eq. 6.

It encompasses a combination of single, interaction, and quadratic effects.

$$Y = +51.7 - 9.6A + 19.4B + 24.3C + 4.14D - 0.84AB + 1.14AC - 0.92AD + 11.2BC + 4.85BD + 2.46CD - 0.941A^2 + 1.94B^2 + 2.22C^2 + 0.46D^2 \quad (6)$$

In the presented equation: Y represents the anticipated BPA removal efficiency in percentage, A signifies the pH, B corresponds to the quantity of nanocomposite (g/L), C denotes the time duration (min), D represents the solution temperature (°C).

Upon analysis of the equation, it becomes evident that an increase in pH hampers the rise in BPA adsorption capacity, while elevating MFZ dosage, contact time, and temperature contributes to a development in adsorption capacity. Comparatively, among the four independent variables, the coefficient corresponding to contact time exhibits the highest value, indicating that time exerts the most significant influence on BPA adsorption capacity. Therefore, the order of influence of the independent variables on BPA adsorption capacity is as follows: contact time > adsorbent dosage > pH > temperature.

Table 2 illustrates the ANOVA results for the quadratic polynomial model in BPA removal, providing insights into the significance of the BBD model design through variance analysis. The high F-value (212.4) and a P-value < 0.0001 indicate the high significance of the quadratic model. Additionally, the lack-of-fit test reveals non-significance with a low F-value and $P < 0.05$, affirming the well-validated nature of the model for BPA adsorption studies.

Regression coefficient (R^2), adequate precision (AP), coefficient of variation (C.V.%), and standard deviation were employed as metrics to evaluate the accuracy and reliability of the experimental results. The AP value of 60.1 exceeds the threshold of 4.0, and the C.V. (%) is 2.46, inferring the reliability of the experimental data. The predicted R^2 and adjusted R^2 values are 0.982 and 0.994, respectively, with a difference smaller than 0.2, signifying that the experimental data are well-suited for further analysis. The model of BPA adsorption onto studied adsorbent exhibited a strong linear correlation, with an R^2 value of 0.995, indicating a close agreement between the actual experimental response and the projected response. This affirms the reliability and applicability of the experimental model.

The examination of residuals involved assessing the normal plot, which illustrates the correlation between percentage probability and internally studentized residuals (see Fig. 5a). A linear curve in the normal distribution of residual values indicates the model's accuracy, while the randomized distribution of residuals signifies the precision of the model. Additionally, an analysis was conducted to prove the association between experimental and predicted q_e, presented in Fig. 5b, and Fig. 5c details the number of experiments conducted. Figure 5b demonstrates that data points closely align with the line, indicating a robust association between experimental and predicted q_e values. These observations strongly support the assertion that the quadratic model is the most appropriate for predicting the response[37].

Within the defined variable range, the effects of parameters on the removal of BPA by MFZ were determined, as illustrated by three-dimensional surface plots and contour lines in Fig. 6a–d.

The removal percentage of BPA by MFZ can be seen to increase as the adsorption dose and system temperature are raised, and as the contact time is extended. Conversely, the removal (%) decreases as the pH level is increased. According to figures, removal percentage experiences an initial increase with the escalating dosage

Source	Sum of squares	df	Mean square	F value	p-value (Prob > F)	
Model	17,452.1	14	16,452.2	212.4	< 0.0001	Significant
A-pH	114.1	1	114.1	15.3	< 0.0001	
B-Dose (g/L)	423.2	1	423.2	45.3	< 0.0001	
Contact time (mg/L)	581.4	1	581.2	63.9	< 0.0001	
D-temperature (°C)	109.2	1	109.2	35.1	0.0001	
AB	21.2	1	21.2	2.75	0.0021	
AC	32.4	1	32.4	1.72	0.981	
AD	18.4	1	18.4	0.472	0.841	
BC	43.6	1	43.6	0.724	0.004	
BD	16.4	1	16.4	5.23	0.741	
CD	9.34	1	9.34	6.37	0.902	
A^2	1.93	1	1.93	11.6	0.006	
B^2	796.4	1	796.1	75.3	< 0.0001	
C^2	984.2	1	984.2	99.2	0.0071	
D^2	1.76	1	1.76	7.44	0.0049	
Residual	144.1	14	14.9			
Lack of fit	95.6	6	9.4	3.94	0.0741	Not significant
Pure error	8.41	4	3.52			
Cor total	21,245.3	29				
Std. Dev = 2.17, C.V. % = 2.46, R^2 = 0.995, Adjusted R^2 = 0.994, Predicted R^2 = 0.982, Adeq precision (AP) = 60.1						

Table 2. Results of ANOVA For BPA degradation by MFZ.

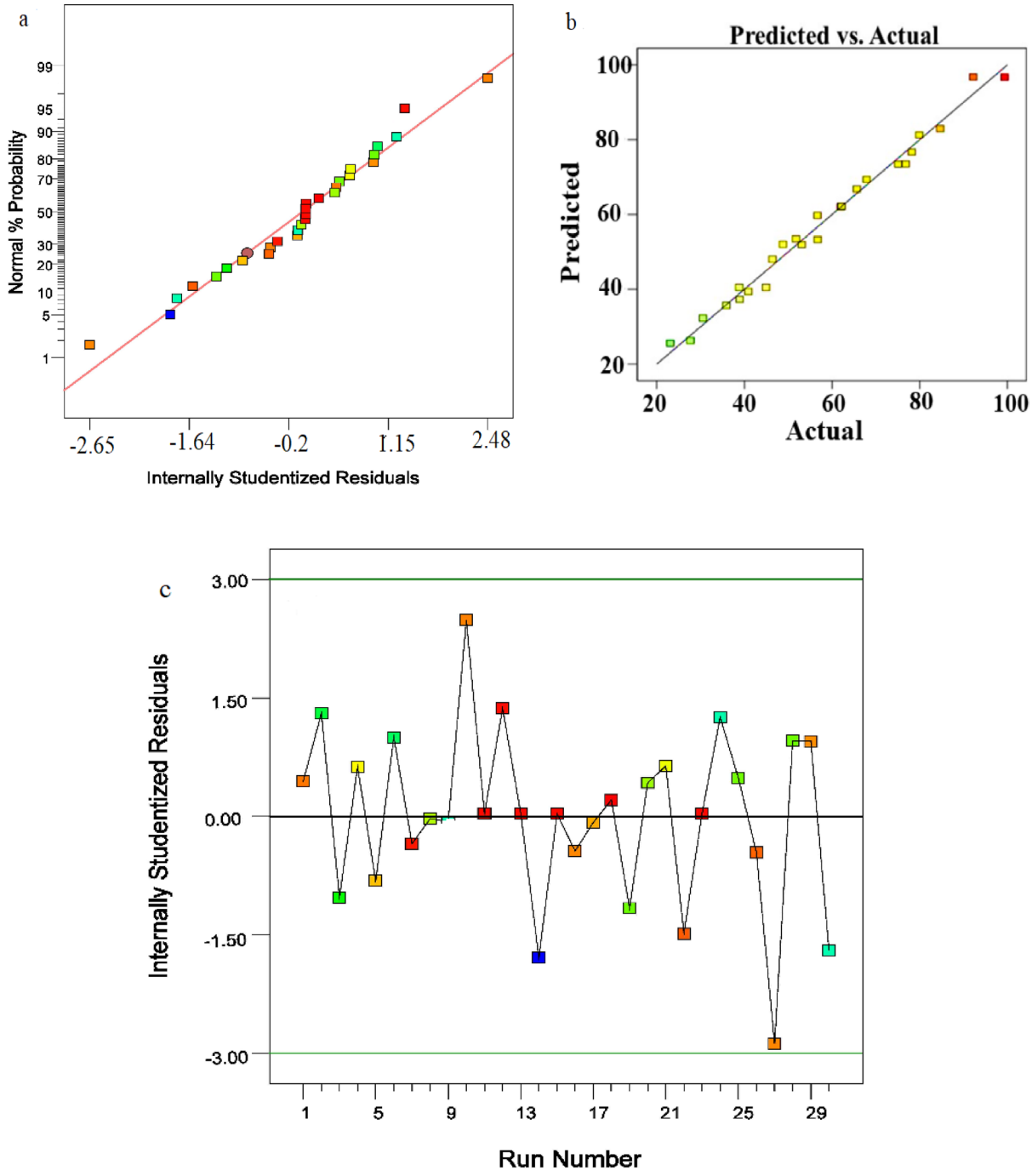

Fig. 5. Normal plot of residuals (**a**); Predicted versus actual plot (**b**); Residuals versus run number (**c**).

of MFZ, primarily due to the augmented surface area[37]. Nevertheless, as the dosage further increases, there is a subsequent decline in removal percentage. This decline is likely caused by the heightened agglomeration of MFZ particles in larger amounts, resulting in a reduction of surface area and, consequently, a decrease in removal percentage[38]. According to figures, removal percentage experiences a decline with an increase in pH. The solution pH is a pivotal factor affecting the removal of BPA. In this particular study, the pH_{zpc} for MFZ is determined to be approximately 6.5 (Fig S1). In essence, when the pH is below the pH_{zpc}, the MFZ surface carries a positive charge, and when the pH exceeds the pH_{zpc}, the MFZ surface becomes negatively charged[15]. In strong acidic media, the production of anionic BPA species and positively charge adsorbent thus increases the force of gravity and increase the amount of adsorption. The removal percentage is diminished in strong alkaline pH due to the repulsion force between the anionic BPA and the negatively charged adsorbent, leading to mutual repulsion[18]. According to figures, the positive effect on BPA removal percentage is observed with rising time, mainly due to the prolonged interaction between the adsorbent and BPA molecules[39]. This extended contact time results in an enhancement of the removal percentage of BPA. Also, with the increase in temperature, the

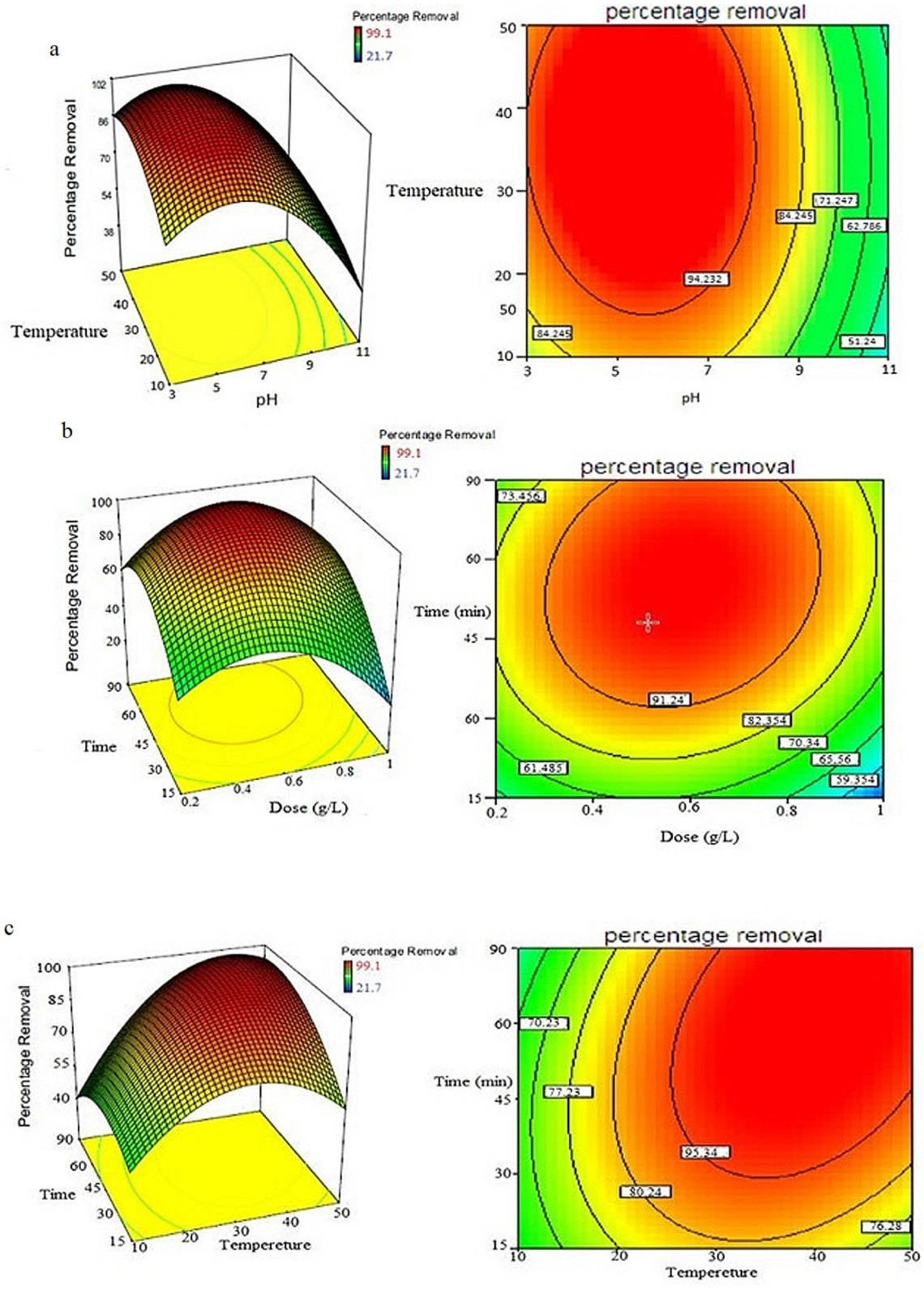

Fig. 6. Response surface plots and contour plots for BPA adsorption (**a**–**d**).

movement of molecules will increase and will cause more collisions between the adsorbent and the pollutant molecules[40].

The optimum conditions for BPA adsorption on MFZ, determined by the model, are a dose of 0.75 g/L, a pH of 6.2, contact time of 72 min, and a temperature of 42 °C, yielding an anticipated percentage removal of 99.1%.

d

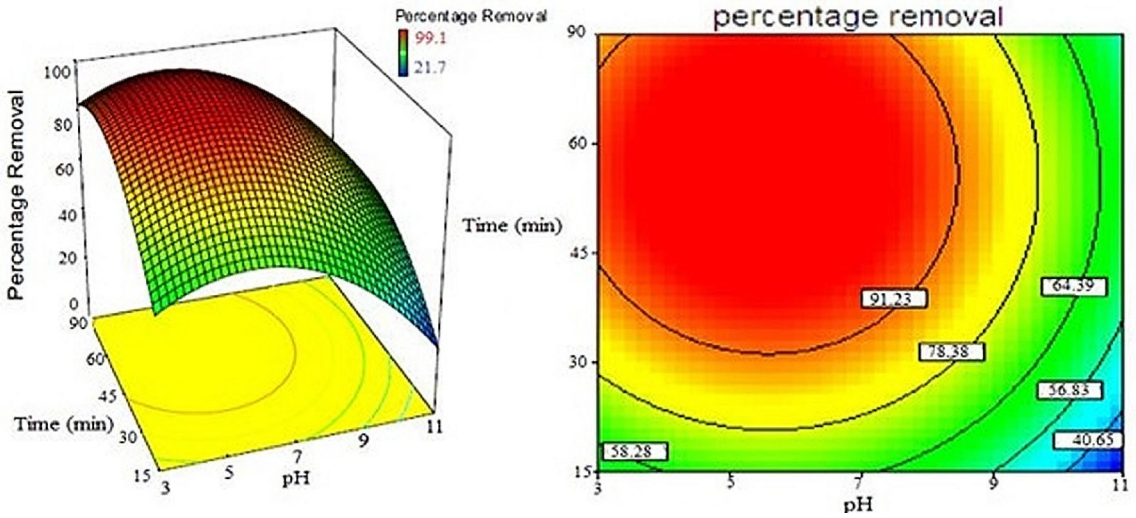

Fig. 6. (continued)

Experimental validation under these conditions showed a percentage removal of 98.9%, deviating only 0.2% from the predicted value. This highlights the effectiveness of the RSM optimization model in analyzing BPA adsorption by MFZ and in establishing the most suitable experimental parameters for the adsorption process.

Kinetics of adsorption

The research in this section focused on studying the impact of contact time on the adsorption of BPA. A 100 mL volumetric flask containing a 100 mg/L concentration of BPA was treated with the adsorbent at a dosage of 0.75 g/L. The experiment was conducted at a temperature of 315 K and a solution pH of 6.2. The flask was agitated for a duration of 10 to 90 min, at a constant speed of 180 rpm.

The observed phenomenon could be a consequence of the concentration differential at the initiation of the reaction, driving BPA to move quickly towards the MFZ surface. At the same time, the adsorbent surface features a significant number of adsorption sites, enhancing the chances of contact and collision between BPA and MFZ[41]. With the progression of the reaction, saturation occurs on the adsorption sites, and the adsorbent surface gains a positive charge due to the mounting attachment of BPA. Consequently, the electrostatic repulsion of free BPA takes place, hindering their contact with the adsorbent surface and resulting in a slowdown in the adsorption process[42].

The equations of the kinetics and their explanations are given in the supplementary section. The summary of fitting parameters for the mentioned kinetic models is provided in Table 3. Notably, the PSO model, with an R^2 value of 0.997, exhibits better performance compared to the PFO model (R^2 = 0.912) in capturing the intricacies of the BPA adsorption data. Emphasizing chemisorption as the exclusive rate-limiting factor, the PSO model implies that chemisorption predominantly regulates the adsorption of BPA onto MFZ[43]. The mechanisms involved in BPA adsorption encompass surface complexation, ion exchange, and electrostatic interactions[44].

Figure 7 presents the fitting results for the IPD models of BPA adsorption on MFZ. As you can see, adsorption happens in three stages. The initial stage takes place within a timeframe of 10 to 30 min, during which the adsorption rate is notably elevated, along with the adsorption rate constant (k_{p1}). The phenomenon of adsorption takes place at discrete surface sites of the adsorbent, which is governed by bulk diffusion[45]. During the second stage, which takes place between 30 and 60 min, the graph's slope decreases, indicating a lower adsorption rate. The reduction in adsorption rate is attributed to the penetration of pollutants to the adsorbent depth from its surface layers[46]. It is noteworthy that the value of k_{p2}, which represents the adsorption rate during this stage, is

PFO	$q_{e\,(cal)}$	95.2	PSO	$q_{e\,(cal)}$	172.2	
	k_1 (min^{-1})	0.047		K_2 (min^{-1})	0.005	
	R^2	0.912		R^2	0.997	
	Stage 1		**Stage 2**		**Stage 3**	
IPD	K_{p1}	22.4	K_{p2}	4.95	K_{p3}	0.541
	C	6.71	C	33.6	C	60.2
	R^2	0.896	R^2	0.942	R^2	0.913

Table 3. Kinetic parameters for the adsorption of BPA on MFZ.

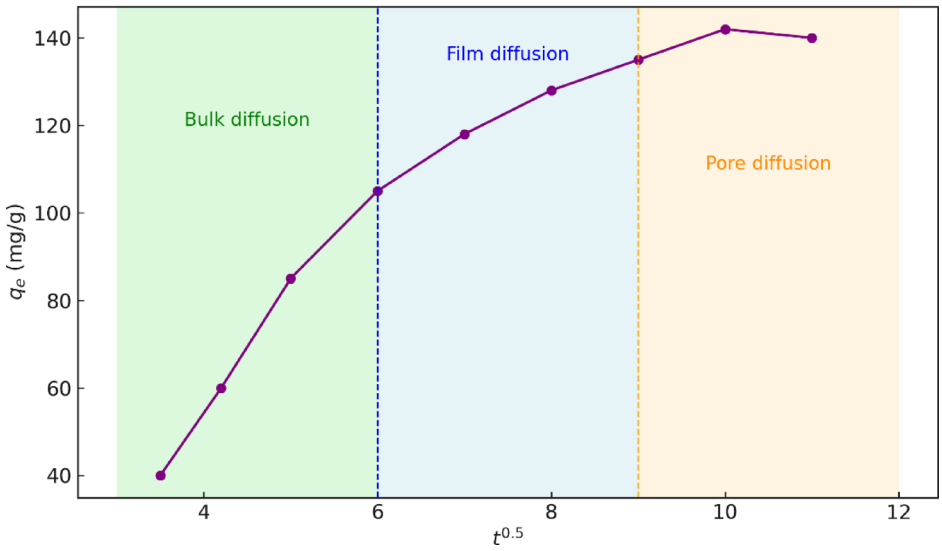

Fig. 7. IPD kinetics for BPA adsorption.

Parameters			Parameters		
Langmuir	Q_m (mg/g)	180.1	Temkin	k_t (L/mg)	1.24
	k_l (L/mg)	0.011		A	61.2
	R^2	0.997		R^2	0.895
Freundlich	k_f (L/mg)	4.48	D-R	Q_m	145.1
	1/n	0.391		E (kJ/mol)	17.2
	R^2	0.912		R^2	0.867

Table 4. Isotherm parameters for the BPA adsorption on MFZ.

lower than k_{p1}, which represents the adsorption rate during the initial stage and is attributed to film diffusion. The onset of the third stage commences after 60 min and can be overlooked due to its sluggish nature. The graph depicting the third stage exhibits a markedly gentle incline, which can be attributed to the phenomenon of pore diffusion, wherein the adsorbate infiltrates the minuscule pores present within it[47].

Adsorption isotherms

For a more thorough understanding of the adsorption mechanism of BPA on MFZ, the data correlating adsorption capacity and the initial concentration of BPA were fitted using several commonly used adsorption isotherm models, including Langmuir, Freundlich, D-R, and Temkin. The equations of the isotherms and their explanations are given in the supplementary section. In Table 4, the parameters pertaining to the adsorption isotherms are outlined. Notably, the Langmuir adsorption isotherm model, characterized by an R^2 value of 0.997, offers a more effective fit to the BPA adsorption results by MFZ than the Freundlich (R^2 = 0.912), D-R (R^2 = 0.867), and Temkin (R^2 = 0.895) models. The uniform distribution of adsorption sites is suggested as the key factor contributing to this superior fit. Furthermore, in accordance with the assumptions of the Langmuir model, the adsorption of BPA is predominantly taking place in monomolecular layers or through a fixed number of identical and energetically equivalent sites on the surface[48,49]. Through the use of the Langmuir isotherm, the maximum adsorption capacity of BPA on MFZ was computed to be 180.1 mg/g The R_L in Langmuir equation was observed to be within the range of zero to one, thereby signifying the validation of adsorption through the Langmuir isotherm. Furthermore, it was observed that the adsorbent under investigation exhibited chemical adsorption of BPA, as evidenced by the fact that less than 17.2 kJ/mol of energy E was derived from the D-R isotherm[50,51].

Thermodynamics of adsorption process

Consideration of temperature is indispensable in the analysis of adsorption processes. To investigate its impact, centrifuge tubes containing 100 mL of a BPA solution at 100 mg/L, with an adsorbent dosage of 0.75 g/L and a pH of 6.2, were subjected to constant temperatures at three different levels (283–323 K). The equations of the thermodynamics and their explanations are given in the supplementary section. The computation of negative values for ΔG^0 (− 2.7, − 3.95, − 5.64, − 7.86 and − 11.86 kJ/mol for 283, 293, 303, 313, and 323 K, respectively) indicates the spontaneous character of adsorption. Elevating the temperature was found to be correlated with a rise in the unfavorable nature of ΔG^0 values[52,53]. Furthermore, the positive $\Delta H°$ (41.3 kJ/mol) for the adsorption

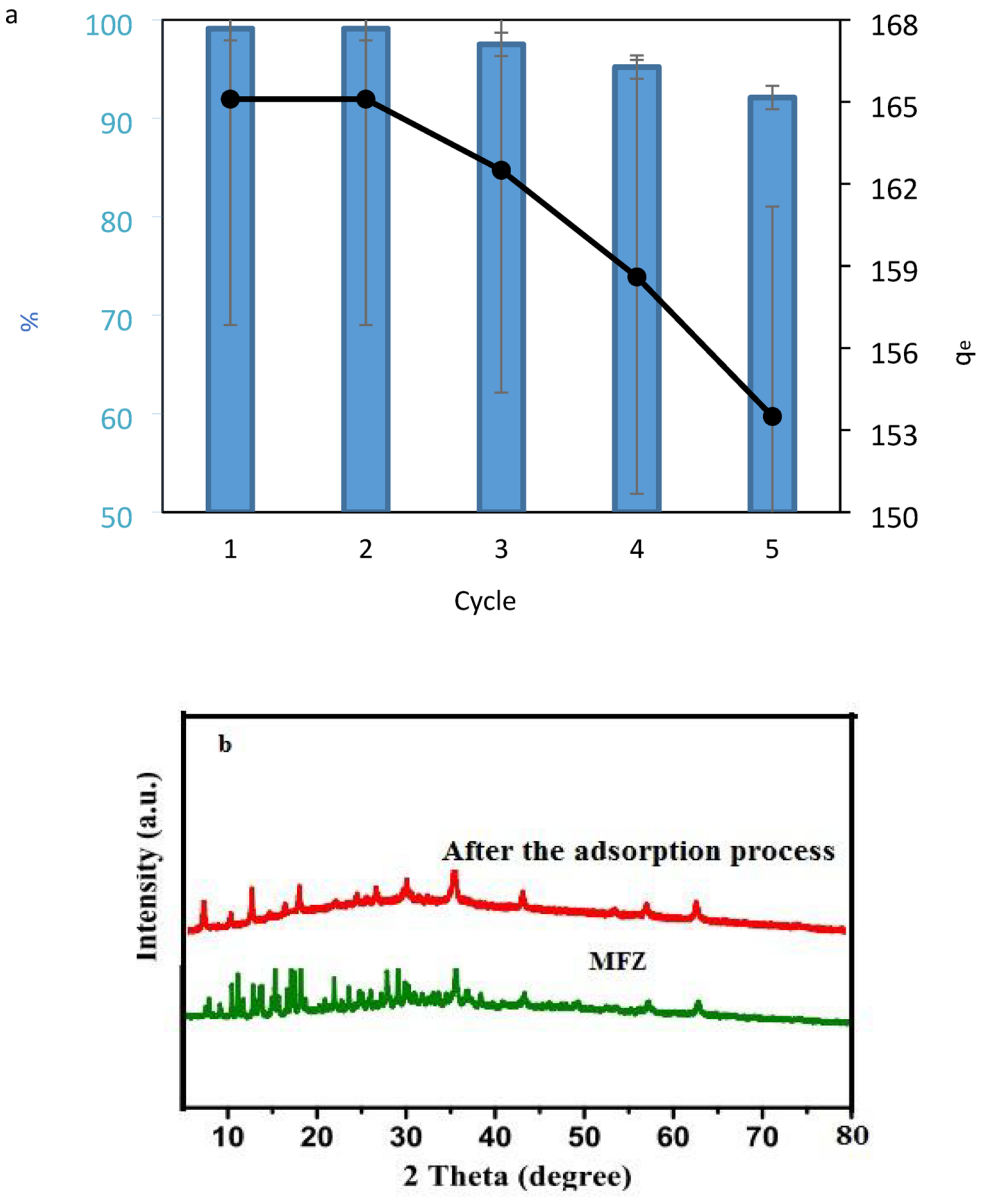

Fig. 8. Reuse cycles of MFZ (**a**); XRD test after adsorption process (**b**); Influence of co-existing ions (**c**).

reaction indicates a heat-absorbing nature, with the BPA adsorption capacity improving as the temperature rises[54]. Higher temperatures accelerate BPA removal. Additionally, the positive ΔS° (0.32 kJ/mol/K) implies that BPA adsorption at the solid–liquid interface is accompanied by a boost in system entropy, indicating a high affinity of the adsorbent for BPA[55,56].

Reusability of MFZ

The reusability of the adsorbent is a crucial factor in assessing the material's economic viability and practical applicability. In this study, 0.75 g/L of MFZ was introduced into a volumetric flask containing 100 mL of a 100-mg/L BPA solution at a pH of 6.2. The volumetric flask was then placed in a thermostatic shaker for 72 min at 42 °C and 180 rpm. The residual BPA concentration was determined through HPLC after separating the magnetic adsorbent using a magnet. To evaluate its reuse performance, the MFZ regeneration was conducted for five cycles (Fig. 8a). Across the five regeneration cycles, the percentage removal of MFZ for BPA experiences a slight decrease. The observed 7% decline in BPA removal efficiency can primarily be ascribed to two factors. First, the progressive reduction in the adsorbent mass during successive adsorption–desorption cycles, wherein approximately 4% of the material is lost in each stage. Second, the partial saturation of active adsorption sites during the desorption process, which consequently diminishes the regeneration capacity and overall performance of the adsorbent[57,58]. Examining the stability of the prepared adsorbent was vital for the adsorption process, and therefore the physicochemical stability of MFZ was verified after five adsorption-desorption processes. Validation of the chemical stability of MFZ involved the application of techniques such as XRD after

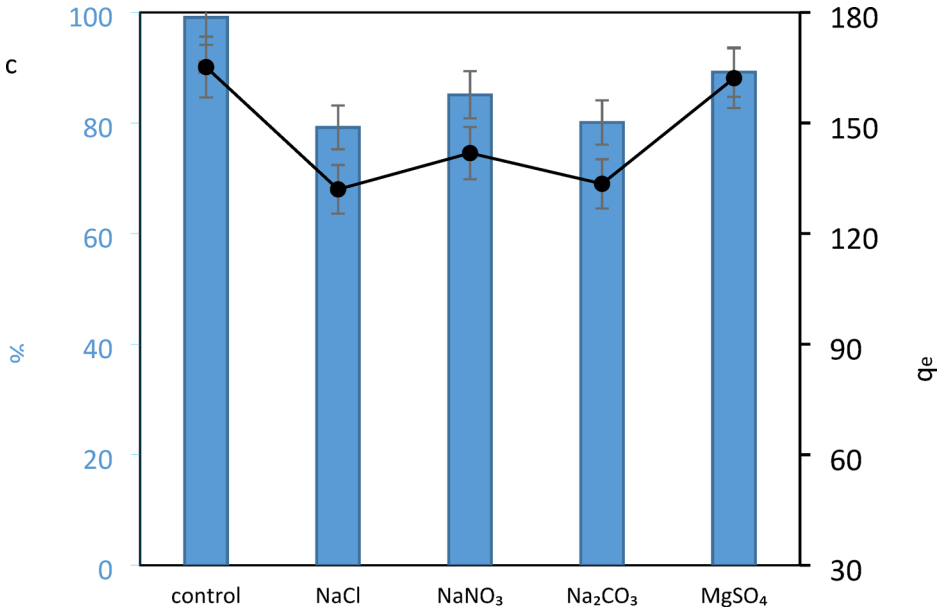

Fig. 8. (continued)

the adsorption-desorption process. As evident from Fig. 8b, despite the presence of diminished crystallinity in certain less significant peaks, the primary peaks linked to the MFZ structure demonstrated a high degree of consistency, validating the enduring chemical stability of MFZ. This suggests that MFZ remains capable of satisfactory adsorption for BPA, even after five regeneration cycles.

Effect of ionic strength

The presence of various ions alongside BPA in the environment introduces a dynamic interplay that can either enhance or impede BPA adsorption. Therefore, understanding the impact of coexisting ions is crucial. The influence of NaCl, Na_2SO_4, Na_2CO_3, and $NaNO_3$ on BPA adsorption was investigated. The variation in percentage removal was assessed when coexisting ionic precursors (100 mg/L) were introduced to a BPA solution, and the results were compared after 72 min (at a pH of 6.2 and a temperature of 315 K). When NaCl, Na_2SO_4, Na_2CO_3, and $NaNO_3$ were introduced, the adsorption efficiency of BPA by MFZ faced varying degrees of hindrance (Fig. 8c). This hindrance increased with the concentration of ions, indicating a competitive relationship between these ions and BPA for adsorption sites. Consequently, the adsorption capacity of BPA was reduced. Additionally, SO_4^{-2}, Cl^-, CO_3^{-2}, and NO_3^- ions were found to be adsorbed on the positively charged surface of the adsorbent. This led to electrostatic repulsion between BPA and the adsorbent surface, impeding interactions between BPA and adsorption sites and contributing to a lowering of adsorption capacity[59].

Performance of MFZ in real wastewater

To further evaluate the practical applicability of the synthesized adsorbent, a preliminary adsorption experiment was conducted using real wastewater collected from a thermal paper recycling facility. The raw wastewater exhibited an initial pH of 5.0 and a COD of 2700 mg/L, with bisphenol A (BPA) identified as one of the main pollutants. The sample was filtered and treated with MFZ under laboratory conditions (adsorbent dosage 1 g/L, contact time 120 min, pH 5.0, shaking at 150 rpm, and room temperature 25 ± 2 °C). The COD was measured at different time intervals to assess the reduction of organic load. The results demonstrated that the COD removal efficiency after 30, 60, and 120 min of contact was 13.1%, 32.7%, and 66.7%, respectively. These findings indicate that MFZ can significantly reduce the organic load of real wastewater containing BPA and other coexisting pollutants. Compared with synthetic BPA solutions, where MFZ achieved over 98% removal efficiency under optimized laboratory conditions within 72 min, the efficiency in real wastewater was markedly lower. This decline can be ascribed to the competitive adsorption of natural organic matter and coexisting ions, which occupy the active sites of MFZ and restrict BPA uptake. Nevertheless, achieving a COD removal of approximately 67% highlights the potential of MFZ for real-world wastewater treatment applications, although its performance is less efficient than under idealized laboratory conditions.

Adsorption mechanisms

The adsorption of BPA onto the MFZ nanocomposite can be ascribed to multiple cooperative interactions between the functional groups of BPA and the active sites of the adsorbent. At the experimental pH (~ 6.2), BPA molecules exist predominantly in their neutral form, as the pKa values of BPA (~ 9–10) are higher than the solution pH. Under such conditions, electrostatic attraction plays only a minor role, while non-electrostatic pathways govern the uptake. Firstly, hydrogen bonding is expected to play a dominant role. The surface –OH groups originating from Fe–O terminations in the Fe_2O_4 core and the Zn–N moieties of the ZIF-8 framework

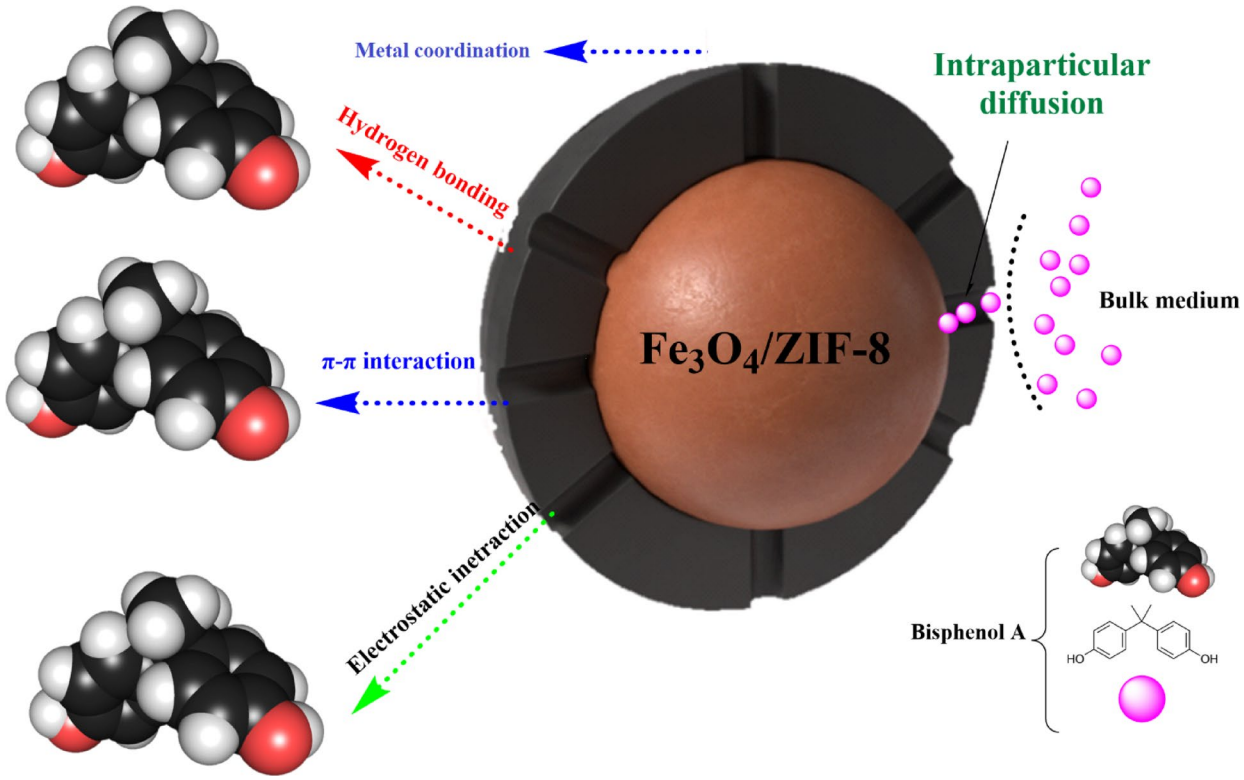

Fig. 9. Adsorption mechanism of BPA onto MFZ.

can act as hydrogen-bond donors and acceptors for the phenolic –OH groups of BPA. The broad O–H vibration observed in the pristine material confirms the presence of accessible hydroxyl species, which may serve as anchoring sites for BPA molecules. Secondly, π–π stacking interactions contribute significantly to molecular affinity. The aromatic rings of BPA can interact with the conjugated π-system of the 2-methylimidazolate linkers in ZIF-8. Such stacking effects increase the stabilization of BPA at the interface and complement the hydrogen bonding, thereby enhancing the adsorption capacity[60]. Thirdly, weak coordination or surface complexation between BPA and the exposed metal sites of MFZ is also plausible. The phenolic oxygen atoms of BPA can coordinate to Zn^{2+} centers in the ZIF-8 shell or to Fe sites partially exposed from the Fe_2O_4 core. The presence of these metal species, as confirmed by XPS characterization of the pristine composite, indicates that such interactions can occur and further anchor BPA molecules on the surface. In addition, the pore structure of ZIF-8 plays a crucial role. BET analysis demonstrated that MFZ possesses a high specific surface area (~ 421 m^2/g) and a pore size distribution in the 3–10 nm range, which is compatible with the molecular dimensions of BPA. This structural feature facilitates pore-filling and hydrophobic confinement, allowing BPA molecules to diffuse into the porous channels and be retained by van der Waals and size-matching effects. The multiphasic IPD model obtained from kinetic fitting further supports the contribution of both surface interactions and internal pore diffusion. The adsorption kinetics fit well to a PSO model, indicating that chemisorption is a rate-controlling step, while the Langmuir isotherm suggests monolayer adsorption on homogeneous sites. The calculated mean free energy (E ≈ 17.2 kJ/mol, DR model) further supports the involvement of strong, specific interactions beyond simple physisorption [61]. . Together, these findings confirm that hydrogen bonding, π–π interactions, weak coordination, and pore confinement act synergistically to achieve rapid uptake and a very high removal efficiency (> 98%). Overall, the superior performance of MFZ arises from the combination of chemical interactions at Zn/Fe and hydroxyl sites, stabilization by aromatic stacking, and confinement within the porous ZIF-8 framework. These mechanisms collectively explain the observed adsorption behavior and highlight the potential of MFZ as a highly effective adsorbent for the removal of BPA and related endocrine-disrupting contaminants. The mechanism diagram is depicted in Fig. 9.

Conclusion

Utilizing the BBD model, this research effectively explored the influence of critical process parameters on the studied process and achieved optimized BPA removal using MFZ. The quadratic model suggested by the BBD showcased a remarkable agreement between predicted and experimental values, indicating minimal errors. Following the optimization process, the study identified optimal conditions, resulting in a 99.1% removal of BPA ions under specific parameters: pH of 6.2, contact time of 72 min, adsorbent dose of 0.75 g/L, and temperature of 315 K. The findings of this study demonstrate that MFZ nanocomposites are not only effective adsorbents under controlled laboratory conditions, but also hold strong potential for practical applications in wastewater treatment. Their high surface area, abundant active sites, and excellent adsorption capacity enable the efficient

removal of endocrine-disrupting compounds such as BPA from aqueous environments. Moreover, the magnetic properties of MFZ allow for simple and rapid recovery with an external magnetic field, reducing operational costs and facilitating reuse in multiple treatment cycles. In addition, efforts should be made to improve regeneration strategies and develop environmentally friendly desorption methods to extend the adsorbent's lifespan and reduce operational costs. Expanding the scope of research to evaluate MFZ for the removal of other endocrine-disrupting compounds, pharmaceuticals, dyes, and heavy metals could further establish its versatility in water treatment. Integrating MFZ adsorption with complementary treatment technologies, such as advanced oxidation processes, photocatalysis, or membrane systems, may also enhance overall efficiency and ensure compliance with strict water quality regulations. Finally, comprehensive cost–benefit and life-cycle assessments are essential to evaluate the economic feasibility, scalability, and sustainability of MFZ production and application, thereby facilitating its transition from laboratory success to large-scale environmental deployment

Data availability

The datasets used and/or analysed during the current study available from the corresponding author on reasonable request.

Received: 8 July 2025; Accepted: 24 September 2025
Published online: 30 October 2025

References

1. Diyanati, R. A., Yousefi, Z. & Cherati, Y. J. The ability of Azolla and lemna minor biomass for adsorption of phenol from aqueous solutions. *J. Mazand Uni Med. Sci.* **23** (106), 141–146 (2013).
2. Zhao, X., Du, P. & Cai, Z. Photocatalysis of bisphenol A by an easy-settling titania/titanate composite: Effects of water chemistry factors, degradation pathway and theoretical calculation. *Environ. Pollut.* **232**, 580–590 (2018).
3. Altin, I., Ma, X. & Boffa, V. Hydrothermal Preparation of B-TiO_2-graphene oxide ternary nanocomposite, characterization and photocatalytic degradation of bisphenol A under simulated solar irradiation. *Mater. Sci. Semicond. Process.* **123**, 105591 (2021).
4. Bhatnagar, A. & Anastopoulos, I. Adsorptive removal of bisphenol A (BPA) from aqueous solution: A review. *Chemosphere* **168**, 885–902 (2017).
5. Da Silva, J. C. C., Reis Teodoro, J. A. & Afonso, D. C. F. Photodegradation of bisphenol A in aqueous medium: Monitoring and identification of by-products by liquid chromatography coupled to high-resolution mass spectrometry. *Rapid Commun. Mass. Spectrom.* **28**, 987–994 (2014).
6. Ďurovcová, I., Kyzek, S. & Fabová, J. Genotoxic potential of bisphenol A: A review. *Environ. Pollut.* **306**, 119346 (2022).
7. Fu, X., Yang, R. & Zhou, G. New progress in photocatalytic degradation of bisphenol A as representative endocrine disrupting chemicals. *Curr. Opin. Green. Sustain. Chem.* **35**, 100629 (2021).
8. Fukahori, S., Ichiura, H., Kitaoka, T. & Tanaka, H. Photocatalytic decomposition of bisphenol A in water using composite TiO_2-zeolite sheets prepared by a papermaking technique. *Environ. Sci. Technol.* **37**, 1048–1051 (2023).
9. Godiya, C. B. & Park, B. J. Removal of bisphenol A form wastewater by physical, chemical and biological remediation techniques. A review. *Environ. Chem. Lett.* **20**, 1801–1837 (2022).
10. Jhones dos Santos, A., Sirés, I. & Brillas, E. Removal of bisphenol A form acidic sulfate medium and urban wastewater using persulfate activated with electroregenerated Fe^{2+}. *Chemosphere* **263**, 128271 (2021).
11. Jia, J., Liu, D. & Wang, Q. Comparative study on bisphenols oxidation via TiO_2 photocatalytic activation of peroxymonosulfate: Effectiveness, mechanism and pathways. *J. Hazard. Mater.* **424**, 127434 (2022).
12. Naganathan, K. K., MohdFaizal, A. N., AhmadZaini, M. A. & Ali, A. Adsorptive removal of bisphenol a form aqueous solution using activated carbon from coffee residue. *Mater. Today Proc.* **47**, 1307–1312 (2021).
13. Soni, H. & Padmaja, P. Palm shell based activated carbon for removal of bisphenol A: An equilibrium, kinetic and thermodynamic study. *J. Porous Mater.* **21**, 275–284 (2014).
14. Wang, J. & Zhang, M. Adsorption characteristics and mechanism of bisphenol A by magnetic Biochar. *Int. J. Environ. Res. Public. Health.* **17**, 1075 (2020).
15. Wang, Y., Pang, Y., Yang, Y. & Shen, X. Facile synthesis of recyclable magnetic covalent organic frameworks for adsorption of bisphenol A form aqueous solution. *J. Porous Mater.* **29**, 1411–1421 (2022).
16. Bhatia, D. & Datta, D. Removal of bisphenol A using amine-modified magnetic multiwalled carbon nanotubes: Batch and column studies. *J. Chem. Eng. Data*. **64**, 2877–2887 (2019).
17. Qingxiang, Z., Yuqin, W., Junping, X. & Huili, F. Fabrication and characterisation of magnetic graphene oxide incorporated Fe_3O_4@polyaniline for the removal of bisphenol A, t-octyl-phenol, and α-naphthol from water. *Sci. Rep.* **7**, 11316 (2017).
18. Fuzil, N. S., Othman, N. H., Ab Jamal, N. & Mustapa, A. N. Bisphenol A adsorption from aqueous solution using graphene oxide-alginate beads. *J. Polym. Environ.* **30**, 597–612 (2022).
19. Lu, F., Lin, J., Lin, C. & Qi, G. Heteroporous 3D covalent organic framework-based magnetic nanospheres for sensitive detection of bisphenol A. *Talanta* **231**, 122343 (2021).
20. Wei, D., Li, J., Chen, Z. & Liang, L. Understanding bisphenol-A adsorption in magnetic modified covalent organic frameworks: Experiments coupled with DFT calculations. *J. Mol. Liq.* **301**, 112431 (2022).
21. Balarak, D., Mostafapour, F. K., Lee, S. M. & Jeon, C. Adsorption of bisphenol A using dried rice husk: Equilibrium, kinetic and thermodynamic studies. *Appl. Chem. Eng.* **30**, 316–323 (2019).
22. Balarak, D. Kinetics Isotherm and thermodynamics studies on bisphenol A adsorption using barley husk. *Int. J. Chem. Tech. Res.* **9**, 681–690 (2016).
23. Zazouli, M. A., Mahdavi, Y. & Bazrafshan, E. Phytodegradation potential of bisphenol A from aqueous solution by Azolla filiculoides. *J. Environ. Health Sci. Eng.* **12**, 66 (2014).
24. Al-Musawi, T. J., Mengelizadeh, N., Ganji, F. & Wang, C. Preparation of multi-walled carbon nanotubes coated with CoFe2O4 nanoparticles and their adsorption performance for Bisphenol A compound. *Adv. Powder Technol.* **33** (2), 103438 (2022).
25. Dianati, R. A. et al. Photocatalytic degradation of bisphenol A by GO-TiO_2 nanocomposite under ultraviolet light: Synthesis, effect of parameters and mineralisation. *Int. J. Environ. Anal. Chem.* **104**, 5065–5082 (2022).
26. Zhou, Y., Lu, P. & Lu, J. Application of natural biosorbent and modified peat for bisphenol a removal from aqueous solutions. *Carbohydr. Polym.* **88**, 502–508 (2012).
27. Dong, Y., Wu, D. & Chen, X. Adsorption of bisphenol A form water by surfactant-modified zeolite. *J. Colloid Interface Sci.* **348**, 585–590 (2010).
28. Jian, M., Liu, B., Zhang, G., Liu, R. & Zhang, X. Adsorptive removal of arsenic from aqueous solution by zeolitic imidazolate framework-8 (ZIF-8) nanoparticles. *Colloids Surf. A*. **465**, 67–76 (2015).

29. Lee, Y. R., Do, X. H., Cho, K. Y., Jeong, K. & Baek, K. Y. Amine-functionalized zeolitic imidazolate framework-8 (ZIF-8) nanocrystals for adsorption of radioactive iodine. *ACS Appl. Nano Mater.* **3** (10), 9852–9861 (2020).
30. Hajializadeh, A., Ansari, M., Foroughi, M., Jahani, S. & Kazemipour, M. Zeolite imidazolate framework nanocrystals electrodeposited on stainless steel fiber for determination of polycyclic aromatic Hydrocarbons. Iranian. *J. Chem. Chem. Eng.* **41** (2), 368–379 (2022).
31. Jiang, X. et al. Magnetic metal-organic framework (Fe_3O_4@ ZIF-8) core-shell composite for the efficient removal of Pb (II) and Cu (II) from water. *J. Environ. Chem. Eng.* **9** (5), 105959 (2021).
32. El-Desouky, M. & El-Bindary, A. Magnetic metal-organic framework (Fe_3O_4@ZIF-8) nanocomposites for adsorption of anionic dyes from wastewater. *Inorg. Nano-Met Chem.* **54**, 81–95 (2024).
33. Qu, Y., Qin, L., Liu, X. & Yang, Y. Magnetic Fe_3O_4/ZIF-8 composite as an effective and recyclable adsorbent for phenol adsorption from wastewater. *Sep. Purif. Technol.* **294**, 121169 (2022).
34. Kyzas, G. Z., McKay, G., Al-Musawi, T. J. & Saleh, S. Removal of benzene and toluene from synthetic wastewater by adsorption onto magnetic zeolitic imidazole framework nanocomposites. *Nanomaterials* **12** 3049. (2022).
35. Al-Hawary, S. I. S., Rahimpoor, R., Rahmani, A. & Romero-Parra, R. M. Enhanced sonophotocatalytic degradation of acid red 14 using Fe_3O_4@SiO_2/PAEDTC@MIL-101 (Fe) based on Metal-Organic framework. *Catalysts* **13** (2), 411 (2023).
36. Wu, Y. et al. Magnetic metal-organic frameworks (Fe_3O_4@ ZIF-8) composites for U (VI) and Eu (III) elimination: Simultaneously achieve favorable stability and functionality. *Chem. Eng. J.* **378**, 122105 (2019).
37. Brahmi, L., Kaouah, F. & Boumaza, S. Response surface methodology for the optimization of acid dye adsorption onto activated carbon prepared from wild date stones. *Appl. Water Sci.* **9**, 171. https://doi.org/10.1007/s13201-019-1053-2 (2019).
38. Nguyen, T. T. T., Hoang, D. & Nguyen, D. T. C. Adsorptive optimization of crystal Violet dye using central composite rotatable design and response surface methodology: Statistical Analysis, kinetic and isotherm studies. *Arab. J. Sci. Eng.* **48**, 8835–8848 (2023).
39. Hussien Hamad, M. T. M. Optimization study of the adsorption of malachite green removal by MgO nano-composite, nano-bentonite and fungal immobilization on active carbon using response surface methodology and kinetic study. *Environ. Sci. Eur.* **35**, 26 (2023).
40. Dargahi, A., Samarghandi, M. R. & Shabanloo, A. Statistical modeling of phenolic compounds adsorption onto low-cost adsorbent prepared from aloe vera leaves wastes using CCD-RSM optimization: Effect of parameters, isotherm, and kinetic studies. *Biomass Conv. Bioref.* **13**, 7859–7873 (2023).
41. Sharma, A. K. et al. RSM-CCD optimized sodium alginate/gelatin based ZnS-nanocomposite hydrogel for the effective removal of biebrich scarlet and crystal violet dyes. *Int. J. Biol. Macromol.* **129**, 214–226 (2019).
42. Takabi, A. S., Shirani, M. & Semnani, A. Apple stem as a high performance cellulose based biosorbent for low cost and eco-friendly adsorption of crystal violet from aqueous solutions using experimental design: Mechanism, kinetic and thermodynamics. *Environ. Technol. Innov.* **24**, 1010947 (2024).
43. Essekri, A. et al. Enhanced adsorptive removal of crystal violet dye from aqueous media using citric acid modified red-seaweed: Experimental study combined with RSM process optimization. *J. Dispers Sci. Technol.* **43**, 1359–1372 (2024).
44. Ghazali, A., Shirani, M., Semnani, A., Zare-Shahabadi, V. & Nekoeinia, M. Optimization of crystal violet adsorption onto date palm leaves as a potent biosorbent from aqueous solutions using response surface methodology and ant colony. *J. Environ. Chem. Eng.* **6**, 3942–3950 (2024).
45. Mojoudi, N., Mirghaffari, N. & Soleimani, M. Phenol adsorption on high microporous activated carbons prepared from oily sludge: Equilibrium, kinetic and thermodynamic studies. *Sci. Rep.* **9**, 19352. https://doi.org/10.1038/s41598-019-55794-4 (2019).
46. Ghafari, M., Cui, Y. & Alali, A. Phenol adsorption and desorption with physically and chemically tailored porous polymers: Mechanistic variability associated with hyper-cross-linking and amination. *J. Hazard. Mater.* **361**, 162–168 (2019).
47. Tazik, M., Dehghani, M. H. & Yaghmaeian, K. 4-Chlorophenol adsorption from water solutions by activated carbon functionalized with amine groups: Response surface method and artificial neural networks. *Sci. Rep.* **13**, 7831. https://doi.org/10.1038/s41598-023-35117-4 (2023).
48. Sharma, S. Activated carbon adsorbent derived from waste biomass, Croton caudatus for efficient removal of 2-chlorophenol from aqueous solution: Kinetics, isotherm, thermodynamics and DFT simulation. *Chem. Eng. Res. Des.* **190**, 777 (2023).
49. Dehghani, M. H., Salari, M. & Karri, R. R. Process modeling of municipal solid waste compost Ash for reactive red 198 dye adsorption from wastewater using data driven approaches. *Sci. Rep.* **11**, 11613. https://doi.org/10.1038/s41598-021-90914-z (2021).
50. Ma, X., Zhao, S., Tian, Z., Duan, G. & Pan, H. MOFs Meet wood: Reusable magnetic hydrophilic composites toward efficient water treatment with super-high dye adsorption capacity at high dye concentration. *Chem. Eng. J.* **446**, 136851. https://doi.org/10.1016/j.cej.2022.136851 (2022).
51. Hsu, C. Y., Saleh, E. A. M. & Moharam, M. M. Optimization of pyrocatechol and p-cresol adsorption onto a composite of chitosan and polyacrylamide incorporated with zeolitic imidazolate Framework-8. *Sci. Rep.* **15**, 22298. https://doi.org/10.1038/s41598-025-07613-2 (2025).
52. Yilmaz, M., Al-Musawi, T. J. & Saloot, M. K. Synthesis of activated carbon from lemna minor plant and magnetized with iron (III) oxide magnetic nanoparticles and its application in removal of Ciprofloxacin. *Biomass Conv Bioref.* **14**, 649–662. https://doi.org/10.1007/s13399-021-02279-y (2024).
53. Al-Musawi, T. J., Mengelizadeh, N. & Al Rawi, O. Capacity and modeling of acid blue 113 dye adsorption onto chitosan magnetized by Fe_2O_3 nanoparticles. *J. Polym. Environ.* **30**, 344–359. https://doi.org/10.1007/s10924-021-02200-8 (2022).
54. Balarak, D., Abasizdeh, H., Jalalzayi, Z., Rajiv, P. & Vanathi, P. Batch adsorption of acid blue 113 dye from aqueous solution using surfactant-modified zeolite. *Indian J. Environ. Prot.* **40** (9), 927–933 (2020).
55. Al-Ha-Wary, S. I. S., Gupta, R., Sapaev, I. B. & Oudaha, K. H. Efficient removal of Amoxycillin antibiotics onto magnetic graphene oxide: Adsorption performance, mechanism, and regeneration exploration. *Inter J. Environ. Anal. Chem.* **105**, 558–580 (2023).
56. Varnaseri, M., Motahari Zadeh, Z., Abdolmohammadi, F., Isotherm, N. & Linear & Kinetic, and thermodynamic behavior of Safranine T adsorption using porous geopolymer prepared from coal fly Ash wastes. *Water Conserv. Sci. Eng.* **9**, 45. https://doi.org/10.1007/s41101-024-00279-3 (2024).
57. Mostafapour, F. K., Miri, A. & Khatibi, A. D. Survey of Fe3O4 magnetic nanoparticles modified with sodium Dodecyl sulfate for removal P-Cresol and Pyrocatechol from aqueous solutions. *Biointerface Res. Appl. Chem.* **13** (6), 554 (2023).
58. Mohebbi, S. & Khatibi, A. Endocrine disruptor (17 β-estradiol) removal by Poly pyrrole-based molecularly imprinted polymer: Kinetic, isotherms and thermodynamic studies. *Appl. Water Sci.* **15**, 43 (2025).
59. Mahvi, A. H. & Mostafapour, F. K. Biosorption of Tetracycline from aqueous solution by Azolla filiculoides: Equlibrium kinetic and thermodynamic studies. *Fresenius Environ. Bull.* **27**, 5759–5767 (2018).
60. Khatibi, A. D., Mahvi, A. H. & Mengelizadeh, N. Adsorption-desorption of Tetracycline onto molecularly imprinted polymer: Isotherm, kinetics, and thermodynamics studies. *Desal Water Treat.* **230**, 240–251 (2021).
61. Pimentel, C. H., Freire, M. S. & Gómez-Díaz, D. Removal of wood dyes from aqueous solutions by sorption on untreated pine (Pinus radiata) sawdust. *Cellulose* **30**, 4587–4608 (2023).

Acknowledgements

We would like to express our heartfelt appreciation to the of Zahedan University of Medical Sciences for their

generous financial support (IR.ZAUMS.REC.1402.271). The authors extend their appreciation to the Deanship of Scientific Research at King Khalid University for funding this work through the large research group program under grant number (R.G.P.02/709/46).

Author contributions

CYH and EAMS: conceptualization, investigation. NMMA and MA: writing-original draft, visualization. SS: writing-review and editing. AS and KVP: conceptualization, investigation, writing-original draft, visualization. MM and NM: methodology, data analysis. DB: Experimental tests. All authors read and approved the final manuscript.

Declarations

Competing interests

The authors declare no competing interests.

Ethical approval and consent to participate

In this work, no animal and human experiments were involved.

Additional information

Supplementary Information The online version contains supplementary material available at https://doi.org/10.1038/s41598-025-21940-4.

Correspondence and requests for materials should be addressed to D.B.

Reprints and permissions information is available at www.nature.com/reprints.

Publisher's note Springer Nature remains neutral with regard to jurisdictional claims in published maps and institutional affiliations.